ELSEVIER

Journal of Hydrology 183 (1996) 169–190

Journal of Hydrology

Linearized cosimulation of hydraulic conductivity, pressure head, and flux in saturated and unsaturated, heterogeneous porous media

Thomas Harter[a,*], Allan L. Gutjahr[b], T.-C. Jim Yeh[c]

[a]*Department of Land, Air and Water Resources, University of California, Davis, Kearney Agricultural Center, Parlier, CA 95616, USA*

[b]*Office of Research and Economic Development, New Mexico Institute of Mining and Technology, Socorro, NM 87801, USA*

[c]*Department of Hydrology and Water Resources, University of Arizona, Tucsan, AZ 85721, USA*

Received 10 March 1994; revision accepted 1 May 1995

Abstract

An efficient cosimulator is developed for generating both random hydraulic property fields and related flow regimes under either saturated or unsaturated conditions. This cosimulator combines a spectral random field generator, based on the Fast Fourier Transform technique, and first-order perturbation/spectral solutions for flow in saturated and unsaturated porous media. Owing to the first-order approximation of the simulator, flow regimes in several geological media with different variabilities are simulated to investigate the accuracy of the simulator. For mild and moderately heterogeneous geological media, the simulator is found to be very accurate in terms of pressure head field and flux distributions. In addition, the execution time of the simulator is substantially smaller than that of any classical numerical simulator. However, the accuracy of the simulator deteriorates as the geological medium becomes highly heterogeneous.

1. Introduction

The effect of heterogeneity on groundwater flow and transport has been an active research area over the past decade and a half. Past studies have included perturbation techniques (Bakr et al., 1978; Gutjahr et al., 1978; Dagan, 1979; Rubin and Dagan, 1987a,b, 1988, 1989) as well as Monte Carlo studies (Smith and Freeze, 1979a,b;

* Corresponding author.

SSDI 0022-1694(95)02814-5

Ababou et al., 1989; Tompson et al., 1989; Tompson and Gelhar, 1990). The perturbation methods often rely on spectral methods though Green's functions have been used as an alternative approach (Naff and Vecchia, 1987; Rubin and Dagan, 1987a,b).

Flow in heterogeneous unsaturated porous media has been examined by Yeh et al. (1985a,b) and Mantoglou and Gelhar (1987a,b,c) who also applied a perturbation technique.

The spectral perturbation methods and Monte Carlo techniques have been combined in previous work (Van Lent and Kitanidis, 1989; Harter, 1994; Gutjahr et al., 1995). In Gutjahr et al. (1993, 1995) and Harter (1994) the spectral method is used along with linear estimation models (kriging and cokriging) to condition based on various types of data (e.g. transmissivity head, etc.). Harter and Yeh (1993) further show how a spectral approach can be used to develop starting solutions for steady-state unsaturated flow models that will lead to rapidly converging numerical solutions. The combination of spectral and simulation methods appears to be very promising for examination of flow and transport models, for application to real fields and for incorporation of conditioning data.

In this paper we examine cosimulation (random field generation) of hydraulic conductivity, head, and flux under steady-state unsaturated and saturated flow conditions, and we investigate the limits of the linearized approach. Our focal point will be the effect of different input variances on the accuracy of the linearized (perturbation) approach. Normalized mean-squared errors of the heads and fluxes (between linear and non-linear solutions) are computed as a function of the input variance of the log-conductivity field.

The linearized models for both saturated and unsaturated flow are recapped in the next section. The spectral method for generation of random fields (Gutjahr, 1989; Gutjahr et al., 1995) is developed in that section since it is used extensively in our approach. The general cosimulation approach is introduced and the set-up for the general approach is elucidated. In Section 3 the results from cosimulation are presented and compared with full and accurate Monte Carlo simulation. The final section demonstrates an application of the cosimulation procedure to simulate transport in heterogeneous porous media.

2. Model development

2.1. Perturbation analysis

Our investigation in this paper focuses on two-dimensional, steady-state, vertical flow in variably saturated vadose zones and on two-dimensional, steady-state, horizontal flow in fully saturated aquifers. The governing flow equation for both cases with unbounded domains can be expressed as

$$\nabla \cdot [K(\boldsymbol{x}, h) \nabla \phi(\boldsymbol{x})] = 0 \tag{1}$$

where ∇ is the two-dimensional Laplacian operator in x_1, and x_2; in the unsaturated

case, x_1 is vertically downward; boldface letters indicate vectors; $\phi(\boldsymbol{x})$ is the total head, that is,

$$\Phi(\boldsymbol{x}) = -\beta x_1 + h(\boldsymbol{x}) \tag{2}$$

For vertical flow in the vadose zone $\beta = 1$. For the saturated flow case $\beta = 0$. The pressure head is $h(\boldsymbol{x})$ (positive under saturated conditions, negative under unsaturated conditions). K in Eq. (1) denotes the hydraulic conductivity which is assumed to take the form

$$K(\boldsymbol{x}, h) = K_s(\boldsymbol{x}) \exp[\beta\alpha(\boldsymbol{x})h(\boldsymbol{x})] \tag{3}$$

where $K_s(\boldsymbol{x})$ is the saturated hydraulic conductivity, which is assumed locally isotropic, and $\alpha(\boldsymbol{x})$ is the soil pore size distribution parameter. For $\beta = 1$, Eq. (3) becomes Gardner's unsaturated conductivity model (1958).

After a logarithmic transformation and letting $y(\boldsymbol{x}) = \ln K(\boldsymbol{x})$, Eq. (1) becomes

$$\nabla y \cdot \nabla\phi + \nabla^2\phi = 0 \tag{4}$$

All variables depending on $\boldsymbol{x}$ are assumed to be stochastic processes in space or random field variables (RFV). The mean gradient is assumed to be in the x_1 direction and is constant in space, i.e.

$$E[\nabla\phi] = -\boldsymbol{J} = -\begin{bmatrix} J_1 \\ 0 \end{bmatrix} \tag{5}$$

We write $\phi(\boldsymbol{x}) = -\beta x_1 + h(\boldsymbol{x}) = -\beta x_1 + H(\boldsymbol{x}) + h'(\boldsymbol{x})$ and $y(\boldsymbol{x}) = Y(\boldsymbol{x}) + y'(\boldsymbol{x})$, where $H(\boldsymbol{x}) = E[\phi(\boldsymbol{x})] + \beta x_1$, $\nabla[-\beta x_1 + H(\boldsymbol{x})] = -\boldsymbol{J}$, $E[h'(\boldsymbol{x})] = 0$, and $E[y'(\boldsymbol{x})] = 0$. Then Eq. (4) simplifies to

$$\nabla^2 h' + \nabla Y \cdot \nabla h' + \nabla y' \cdot \nabla h' - \boldsymbol{J} \cdot \nabla(Y + y') = 0 \tag{6}$$

In the first-order, linearized perturbation analysis the term $\nabla y' \cdot \nabla h'$ is dropped and

$$\nabla^2 h' + \nabla Y \cdot \nabla h' = \boldsymbol{J} \cdot \nabla(Y + y') \tag{7}$$

The RFV parameters in Eq. (3) are written as $\ln K_s(\boldsymbol{x}) = f(\boldsymbol{x}) = F(\boldsymbol{x}) + f'(\boldsymbol{x})$ and $\ln\alpha(\boldsymbol{x}) = a(\boldsymbol{x}) = A(\boldsymbol{x}) + a'(\boldsymbol{x})$, where again $F(\boldsymbol{x}) = E[f(\boldsymbol{x})]$, $A(\boldsymbol{x}) = E[a(\boldsymbol{x})]$, $E[f'(\boldsymbol{x})] = E[a'(\boldsymbol{x})] = 0$. If the medium is fully saturated, then from Eq. (3) we have the equality $y(\boldsymbol{x}) = f(\boldsymbol{x})$. On the other hand, if the medium is unsaturated, Gardner's $K(h)$ model in Eq. (3) is expanded into

$$y = F + f' + \Gamma \exp(a')(H + h') \tag{8}$$

where we denote $\Gamma = \exp(A)$, which is the geometric mean of α. The exponential peturbation term $\exp(a')$ in Eq. (8) is expanded in a Taylor series. After all terms involving products of two or more perturbation terms are dropped (including second and higher order powers of a' in the Taylor series), the mean $Y(\boldsymbol{x})$ and the perturbation $y'(\boldsymbol{x})$ are written for the general saturated/unsaturated flow case

$$\begin{aligned} y &= F + \beta\Gamma H \\ y' &= f' + \beta\Gamma h' + \beta\Gamma H a' \end{aligned} \tag{9}$$

Then expansion of Eq. (7) with Eq. (9) yields the generalized linear perturbation flow

equation for saturated/unsaturated flow

$$\nabla^2 h' + \nabla(F + \beta\Gamma H) \cdot \nabla h' = \boldsymbol{J} \cdot \nabla(F + \beta\Gamma H + f' + \beta\Gamma h' + \beta\Gamma H a') \tag{10}$$

The RFV f and a are assumed second-order stationary, and consequently F and Γ, like J_1, are constant in space. In the unsaturated vertical flow case ($\beta = 1$), H is also assumed to be second-order stationary, i.e. the mean pressure head is uniform over the entire soil, and water flux therefore driven by gravity ($J_1 = 1$). With Eq. (5) the general flow equation (10) then simplifies to

$$\nabla^2 h' = J_1 \left(\frac{\partial f'}{\partial x_1} + \beta\Gamma \frac{\partial h'}{\partial x_1} + \beta\Gamma H \frac{\partial a'}{\partial x_1} \right) \tag{11}$$

Similar to the analysis by Yeh et al. (1985a), the first-order perturbation of flux can be derived from Darcy's law

$$\boldsymbol{q}(\boldsymbol{x}) = -K(\boldsymbol{x}, h) \nabla \phi(\boldsymbol{x}) \tag{12}$$

where $\boldsymbol{q}$ is the flux or Darcian velocity. Expanding Eq. (12) with Eq. (9), and using perturbation notation, the first-order mean and perturbation of the two flux components q_1 and q_2 are second-order stationary and are

$$\langle q_1 \rangle = -K_m J_1 \tag{13a}$$

$$\langle q_2 \rangle = -K_m J_2 = 0 \tag{13b}$$

$$q_1' = -K_m \left[J_1 (f' + \beta\Gamma h' + \beta\Gamma H a') + \frac{\partial h'}{\partial x_1} \right] \tag{13c}$$

$$q_2' = -K_m \frac{\partial h'}{\partial x_2} \tag{13d}$$

where $K_m = \exp(Y)$. Note that the total flux $\boldsymbol{q} = \langle \boldsymbol{q} \rangle + \boldsymbol{q}'$. The pore velocity is computed by dividing $\boldsymbol{q}$ with the effective water content θ_e (effective porosity in the saturated flow case). For demonstration purposes and simplicity θ_e is here assumed to be spatially homogeneous. For practical applications, θ_e must be computed as a function of h, whereby the independent parameters of such a function may be RFV.

2.2. Spectral analysis and cosimulation

If a process $V(\boldsymbol{x})$ is second-order stationary with mean 0 and covariance function $C_{vv}(\boldsymbol{\xi})$ then there exists a unique (with probability one) complex process $Z(\boldsymbol{u})$ with the following properties

$$V(\boldsymbol{x}) = \int_{-\infty}^{\infty} \exp(i2\pi \boldsymbol{u} \cdot \boldsymbol{x}) \, \mathrm{d}Z(\boldsymbol{u}) \tag{14}$$

$$E[\mathrm{d}Z(\boldsymbol{u}_k) \, \mathrm{d}Z(\boldsymbol{u}_l)] = \begin{cases} S_{vv}(\boldsymbol{u}) \mathrm{d}\boldsymbol{u} & \text{if } \boldsymbol{u} = \boldsymbol{u}_k = \boldsymbol{u}_l \\ 0 & \text{otherwise} \end{cases} \tag{15}$$

$$S_{vv}(\boldsymbol{u}) = \int_{-\infty}^{\infty} \exp(-i2\pi \boldsymbol{u}\cdot\boldsymbol{\xi}) C_{vv}(\boldsymbol{\xi})\, d\boldsymbol{\xi} \tag{16}$$

$$E[dZ(\boldsymbol{u})] = 0 \tag{17}$$

Here we use the convention that multiple integrals and sums are represented in vector notation. Thus

$$\int_{-\infty}^{\infty}\int_{-\infty}^{\infty} G(u_1, u_2)\, du_2 du_1 = \int_{-\infty}^{\infty} G(\boldsymbol{u})\, d\boldsymbol{u} \tag{18}$$

and

$$\sum_{J_1=-N_1}^{M_1}\sum_{J_2=-N_2}^{M_2} g(J_1, J_2) = \sum_{J=-N}^{M} g(J) \tag{19}$$

where

$$\boldsymbol{N} = \begin{pmatrix} N_1 \\ N_2 \end{pmatrix}, \qquad \boldsymbol{M} = \begin{pmatrix} M_1 \\ M_2 \end{pmatrix}.$$

$S_{vv}(\boldsymbol{u})$ is called the spectral density for the process $V(\boldsymbol{x})$ and is a measure of how the variance is spread across the frequency space (designated by $\boldsymbol{u}$). In addition $C_{vv}(\xi)$ can be recovered from the spectral density by the inverse Fourier Transform

$$C_{vv}(\boldsymbol{\xi}) = \int_{-\infty}^{\infty} \exp(i2\pi \boldsymbol{\xi}\cdot\boldsymbol{u}) S_{vv}(\boldsymbol{u})\, d\boldsymbol{u} \tag{20}$$

Discussions and proofs for the spectral representation theorem can be found in Koopmans (1974), Priestley (1981), and Lumley and Panofsky (1964). Important aspects include the uniqueness, and the connections of the dZs and the spectral density $S_{vv}(\boldsymbol{u})$.

Applying the spectral representation (14) and uniqueness to Eq. (11), where f', a', and h' are assumed to be second-order stationary, the first-order flow equation has an explicit solution

$$dZ_h(\boldsymbol{u}) = \frac{-i(2\pi)\boldsymbol{J}\cdot\boldsymbol{u}}{(2\pi u)^2 + i\beta\Gamma 2\pi u_1}\left[dZ_f(\boldsymbol{u}) + \beta\Gamma H dZ_a(\boldsymbol{u})\right] \tag{21}$$

where $u^2 = \boldsymbol{u}\cdot\boldsymbol{u}$. Note that the spectral densities defining the dZ_f and dZ_a processes, and hence the covariance functions of the f and a processes need not be identical.

With the same approach, the spectral representation of the second-order stationary flux perturbation q' can be derived from Eqs. (13c), (13d), and (14)

$$\begin{aligned} dZ_{q1}(\boldsymbol{u}) &= -K_m[dZ_f(\boldsymbol{u}) + \beta\Gamma H dZ_a(\boldsymbol{u}) + (\beta\Gamma + i2\pi u_1)\, dZ_h(\boldsymbol{u})] \\ dZ_{q2}(\boldsymbol{u}) &= -K_m i2\pi u_2 dZ_h(\boldsymbol{u}) \end{aligned} \tag{22}$$

Eqs. (21) and (22) along with the spectral representation (14) form the basis for the cosimulation method. They provide explicit solutions to the first-order flow equation (11) and to the first-order form of Darcy's law (13) given the spectral representation dZ_f and dZ_a of realizations of the f and a random fields. Eqs. (21) and (22) are coupled with an expansion of the integrals into sums, and the sums are then evaluated using a Fast Fourier Transform (FFT, Brigham, 1988).

We now address the question of how to construct the dZ_f and dZ_a processes. For an arbitrary mean 0 second-order stationary process consider the spectral representation and an expansion of the integral

$$V(\boldsymbol{x}) \cong \int_{-U_m}^{U_m} \exp(i2\pi \boldsymbol{u}\cdot\boldsymbol{x})\, dZ(\boldsymbol{u}) \cong \sum_{k=-M}^{M-1} \exp(i2\boldsymbol{u}_k\cdot\boldsymbol{x})\, dZ(u_k) \tag{23}$$

The integrals are truncated at $\boldsymbol{U}_m$ and we further discretize

$$\boldsymbol{x} = (J_1\Delta x_1, J_2\Delta x_2) = \boldsymbol{J}\odot\Delta\boldsymbol{x}$$

where

$$\boldsymbol{a}\odot\boldsymbol{b} = (a_1b_1, a_2b_2) \tag{24}$$

In addition the u_ks are discretized into equi-spaced intervals: either

$$\boldsymbol{u}_k = \boldsymbol{k}\odot\Delta\boldsymbol{u}$$

or

$$\boldsymbol{u}_k = (\boldsymbol{k}+\mathbf{1/2})\odot\Delta\boldsymbol{u} \tag{25}$$

In the applications presented here we use the first form for $\boldsymbol{u}_k$ while the second form is used in Gutjahr et al. (1995): the differences are minimal.

With these choices the expansion in Eq. (23) becomes

$$V[J\odot\Delta\boldsymbol{x}] = \sum_{k=-M}^{M-1} \exp[2\pi i(k_1J_1\Delta\boldsymbol{u}_1\Delta\boldsymbol{x}_1 + k_2J_2\Delta\boldsymbol{u}_2\Delta\boldsymbol{x}_2)]\, dZ[\boldsymbol{k}\odot\Delta\boldsymbol{u}] = \sum_{k=-M}^{M-1} \exp[2\pi i(k_1J_1/2\boldsymbol{M}_1 + k_2J_2/2\boldsymbol{M}_2)]\, dZ[\boldsymbol{k}\odot\Delta\boldsymbol{u}] \tag{26}$$

where

$$\Delta\boldsymbol{u}_1\Delta x_1 = 1/2\boldsymbol{M}_1, \qquad \Delta\boldsymbol{u}_2x_2 = 1/2\boldsymbol{M}_2$$

The sum in Eq. (26) is efficiently evaluated with the FFT. Finally the dZs are constrained so that $V(\boldsymbol{x})$ is real and so that Eqs. (15) and (16) are satisfied in discretized

form. The condition that $V(\boldsymbol{i} \odot \Delta \boldsymbol{x})$ be real is satisfied if

$$\mathrm{d}Z[\boldsymbol{k} \odot \Delta \boldsymbol{u}] = \mathrm{d}Z^*[\boldsymbol{k} \odot \Delta \boldsymbol{u}]$$

for

$$k_1 \neq -M_1, \qquad k_2 \neq -M_2 \tag{27}$$

and

$$\mathrm{d}Z[-\boldsymbol{k} \odot \Delta \boldsymbol{u}] = 0 \quad \text{if either} \quad k_1 = -M_1 \quad \text{or} \quad k_2 = -M_2$$

In addition $\mathrm{d}Z(\mathbf{0})$ is real in this set-up.

To satisfy the conditions in Eq. (27) and $\mathrm{d}Z$s are constructed as follows

$$\mathrm{d}Z[\boldsymbol{k} \odot \Delta \boldsymbol{u}] = [A_{\boldsymbol{k}} + iB_{\boldsymbol{k}}]\,[S_{\mathrm{vv}}(\boldsymbol{k} \odot \Delta \boldsymbol{u})\,\Delta u_1 \Delta u_2]^{1/2} \tag{28}$$

where

$$E[A_{\boldsymbol{k}}] = E[B_{\boldsymbol{k}}] = 0;$$

and

$$\mathrm{Var}(A_{\boldsymbol{k}}) = \mathrm{Var}(B_{\boldsymbol{k}}) = 1/2 \quad \text{for} \quad \boldsymbol{k}_1 > 0, -M_2 - 1 \leq \boldsymbol{k}_2 \leq M_2 - 1$$

To satisfy Eq. (28) we further take the $A_{\boldsymbol{k}}$s and $B_{\boldsymbol{k}}$s to be independent of each other. Under these assumptions it should be noted that by Lyapunov's central limit theorem $V(\boldsymbol{j} \odot \Delta \boldsymbol{x})$ is Gaussian as $\boldsymbol{M}$ approaches infinity (Gutjahr et al., 1995). One could generate non-normal random processes by taking the As and Bs to be uncorrelated but not independent. The practicality of such an approach has not been explored. In this paper our interest is in values of $y(\boldsymbol{x})$ that are normal (namely, $K(\boldsymbol{x})$ is log–normal). For the linearized system, $h(\boldsymbol{x})$ and $\boldsymbol{q}(\boldsymbol{x})$ are then also normal or Gaussian.

The random field generation of f and a based on the FFT algorithm is further discussed in Gutjahr (1989), Gutjahr et al. (1995), and Harter (1994). The FFT based random field generator, where the spectral representations $\mathrm{d}Z_f(\boldsymbol{u})$ and $\mathrm{d}Z_a(\boldsymbol{u})$ are essentially generated as realizations of uncorrelated random numbers (28), provides the additional advantage that random field realizations of f and a need not be transformed into their respective spectral representation to compute the linearized solutions Eqs. (21) and (22). Certain discretization criteria must be met to assure that the truncation and discretization in Eq. (23) leaves it approximately identical to Eq. (14). Grid discretization should be such that at least five grid-points are within one correlation length, and the domain size should be at least ten to 20 correlation lengths (Gutjahr, 1989; Robin et al., 1993). The size of the random field should be even larger if discretization errors are to be avoided in the linearized solution of h, since h has a much longer correlation scale than the RFV f and a. The method is therefore unsuitable for generating relatively small random fields.

In the following section, the linearized solutions h_{L} (FFT of Eq. (21)) and $\boldsymbol{q}_{\mathrm{L}}$ (FFT of Eq. (22)) are compared with the 'exact' non-linear, numerical solutions h_{NL} and $\boldsymbol{q}_{\mathrm{NL}}$, where the numerical model uses the boundary conditions from the linearized, quasi-infinite domain solution. For simplicity, f and a are assumed to be uncorrelated and have identical covariance functions. Field data such as those by Wierenga et al.

(1989) show that f and a are weakly correlated and do not have identical covariance functions. Robin et al. (1993) provide a spectral method for generating weakly correlated random fields of f and a with arbitrary covariance functions, which can be incorporated into the procedure described above.

3. Comparison of linearized solutions with non-linear model

3.1. Computational experiments

Two hypothetical field sites are used for the comparison of the linearized solutions with the non-linear, 'true' solutions: an unsaturated, vertical cross-section of a heterogeneous soil profile, and a saturated, horizontally planar field site (aquifer). Both sites are discretized into a domain with 128^2 grid points with mean flow direction being parallel to the x_1-axis. Gravity flow, i.e. unit mean gradient, $J_1 = 1$, is assumed at the soil site. The mean gradient in the aquifer is set to $J_1 = 0.01$. The effective water content of the soil and the effective porosity of the aquifer are assumed to have negligible spatial variability and are treated as constants throughout the simulated domain. The input random field realizations of f (saturated and unsaturated sites) and a (unsaturated site) have an anisotropic, exponential covariance structure

$$\frac{C_{VV}(\boldsymbol{\xi})}{\sigma_V^2} = \exp\left(-\sqrt{\frac{x_1^2}{\lambda_1^2}+\frac{x_2^2}{\lambda_2^2}}\right) \qquad V = f, a \tag{29}$$

where $C_{VV}(\xi)$ is the covariance function and δ_V^2 is the variance of the RFV $V = f, a$. Although not required by the model, it is here assumed that the covariance functions for f and a have an identical correlation scale λ. Both sites are anisotropic with the anisotropy axes coinciding with the coordinate axes of the simulation grid. In the soil profile, the statistical anisotropy ratio ($\upsilon = \lambda_1/\lambda_2$) is set to 0.5, i.e. the major anisotropy axis is transverse to the mean flow direction. In contrast, the aquifer has a ratio $\upsilon = 2.0$; there, the major anisotropy axis is parallel to mean flow. The distance between two grid points in both dimensions is $0.2\lambda_j$, $j = 1, 2$. Thus, the total length of the simulated domain in the jth direction is 25.6 λ_j. For the soil site, two additional parameters must be defined. The dimensionless geometric mean of α is $\Gamma' = \Gamma\lambda_1 = 1.5$ and the dimensionless mean pressure head $H' = \Gamma H$ is -4.5. Cosimulated, linearized random field realizations of h_L and $\boldsymbol{q}_L$ are obtained for different variances of f and a (see Table 1).

The random field realizations of f and a are used as input to MMOC2 (Yeh et al., 1993), a Galerkin finite element model for solving the variably saturated flow equation (1) and Darcy's law (12). The model uses the Newton–Raphson method for solving the non-linear portion of Eq. (1) and a preconditioned conjugate gradient solver for the resulting linear finite element matrix equation. With h_L as initial solution, MMOC2 converges directly to the non-linear, fully perturbed solution h_{NL}, from which the flux $\boldsymbol{q}_{NL}$ is then computed, also by the finite element method. The

Table 1
Input variance of f and a and resulting variance of y in the eight Monte Carlo simulations

σ_f^2	σ_a^2	σ_y^2
0.09	–	0.09
0.46	–	0.46
0.93	–	0.93
1.86	–	1.86
0.01	0.01	0.11
0.23	0.04	0.58
1.12	0.04	1.13
3.01	0.04	2.41

The first four Monte Carlo simulations are in saturated porous media. The last four simulations in unsaturated porous media.

application of h_L as initial solution or initial guess for a numerical model leads to computationally very efficient steady-state solutions h_{NL}, particularly in the unsaturated case (so-called ASIGNing technique, see Harter and Yeh, 1993). Also, the linearized initial solution provides a random constant head boundary condition for the numerical model. Hence, the numerical model conceptually represents a portion of a semi-infinite random medium.

3.2. *Linearized and non-linear realizations of* h *and* q

Single realizations of analytical, linearized unsaturated head and flux solutions are compared with numerical solutions to study the general, qualitative accuracy of the spectral approach. Harter and Yeh (1993) have shown that the computation of a linearized solution of h is on the order of three magnitudes faster than the finite element computation of actual, non-linear h and $\boldsymbol{q}$ solutions. In the following examples, the CPU-time for computing a single linearized solution h_L and $\boldsymbol{q}_L$ on a 128×128 grid is 3.5 s on an IBM RS6000/560 workstation. Using h_L as initial solution, the CPU-time for the finite element solution h_{NL} and $\boldsymbol{q}_{NL}$ varies between approximately 10^2 s for small input variances and approximately 10^3 s for large input variances. If unsaturated flow solutions were computed without h_L as initial solution, CPU-time would be up to an additional order of magnitude larger.

For small variances in unsaturated hydraulic conductivity ($\sigma_y^2 = 0.1$, unsaturated flow) or in saturated hydraulic conductivity ($\sigma_f^2 = 0.1$, saturated flow), the linearized flow solutions h_L and $\boldsymbol{q}_L$ and the non-linear finite element solutions h_{NL} and $\boldsymbol{q}_{NL}$ are very similar (Fig. 1). The distinguishable areas of low and high values are identical throughout the domain. The different spatial patterns between the h, q_1 and q_2 solutions are caused by the different physical behavior of the three quantities and are well explained by analytically derived correlation functions (Harter, 1994).

For the same variance ratio $\zeta = \sigma_a/\sigma_f$, the input variances of f and a have no impact on the linearized solution other than scaling the actual values of h, q_1, and q_2 proportional to the input variance (see Eqs. (21), (22), (28)). In our experiments, ζ changes slightly, but overall the pattern of the particular linearized realization in

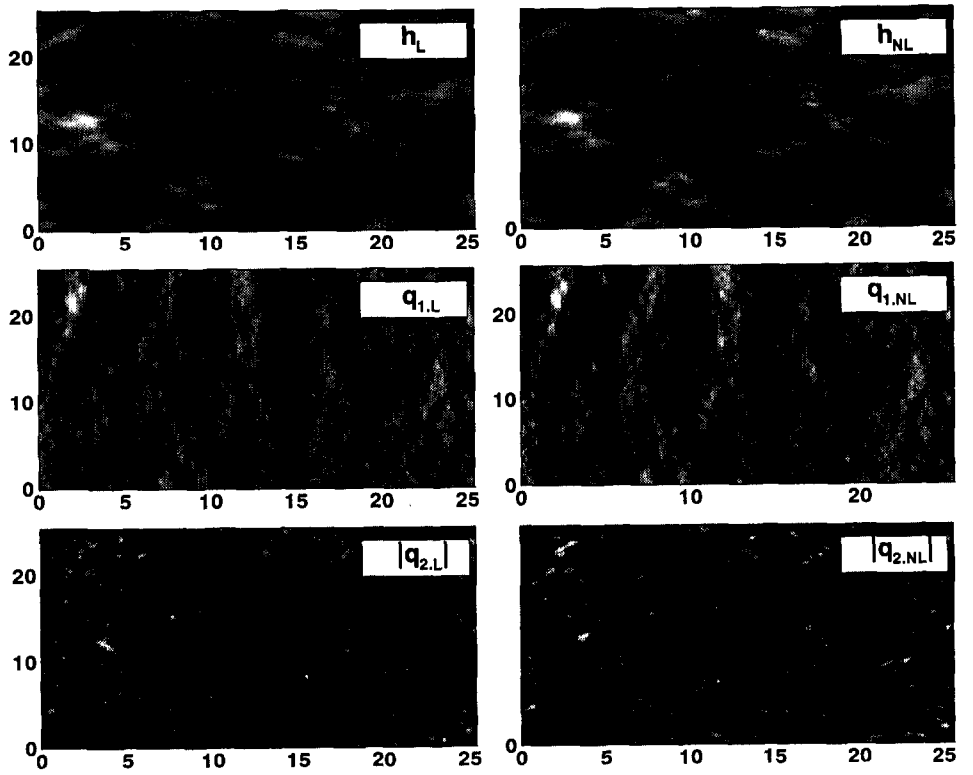

Fig. 1. Unsaturated flow, mild spatial heterogeneity ($\sigma_y^2 = 0.1$): realization of a linearized and non-linear head and flux solution, given the same random field realizations of f and a. The linearized, analytical solutions are in the left column (indicated by subscript L), the non-linear, numerical solutions are in the right column (indicated by subscript NL). The numbers on the axes indicate the dimensionless distances $x_j/\lambda_j, j = 1, 2$. The absolute length ratio of the axes is $x_1/x_2 = 1$. The direction of mean flux is vertically downward. The anisotropy ratio is $\lambda_1/\lambda_2 = 0.5$. Lighter colors represent higher negative pressure (dry areas) and high flux (strong downward flow).

Fig. 1 changes little, when regenerated with the same random number seed at the higher variances indicated in Table 1 (compare Figs. 1 and 2). However, the exact, non-linear solutions of h and $\boldsymbol{q}$ develop very peculiar features at higher input variances ($\sigma_y^2 \geq 0.5$). These are unique to the non-linear solutions and are not captured by the linearized analytical solutions. As shown in Fig. 2 for $\sigma_y^2 = 2.4$, steep vertical gradients develop in the head field with wet areas of low water tension (dark shade) frequently located immediately upstream of very dry areas of high water tension (white areas). This gives the h_{NL} map in Fig. 2 the characteristic 'clouds in the sky' character. In Fig. 3, a longitudinal cross-section of the unsaturated head is shown for realizations with different variances of y (but identical random number seed): at low variances, the analytical and numerical solutions match very closely. As the variance of y increases, slopes where pressure head increases in the positive (downward) x_1 direction (decreasing tension) reduce their angle with respect to x_1.

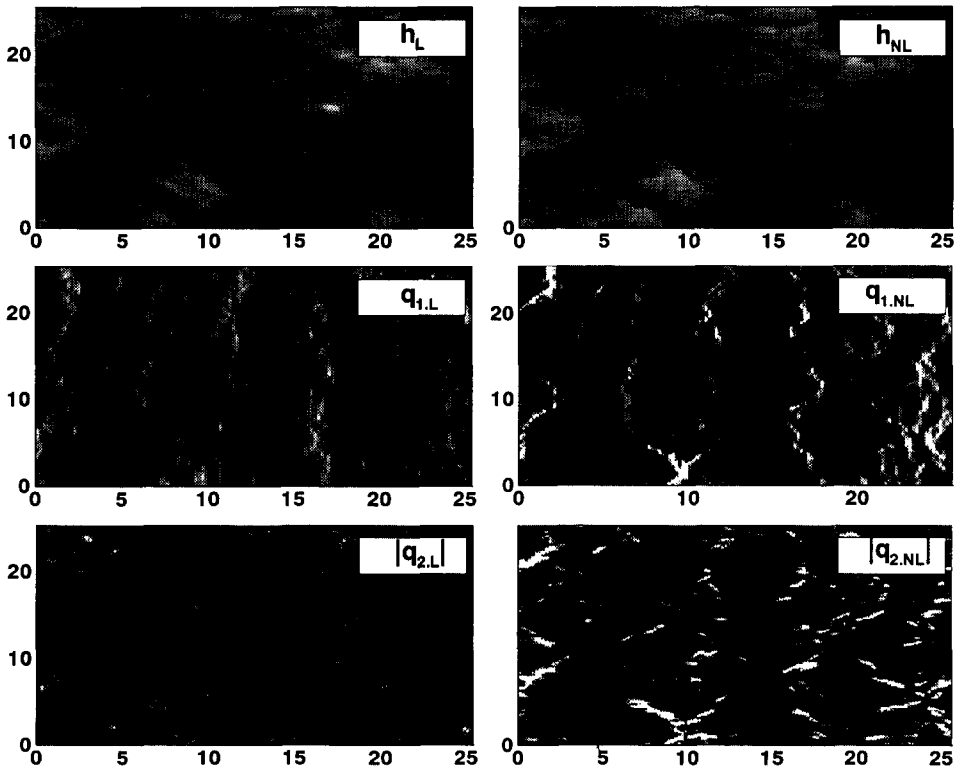

Fig. 2. Unsaturated flow, strong spatial heterogeneity ($\sigma_y^2 = 2.4$): realization of a linearized and non-linear head and flux solution, given the same random field realizations of f and a. The random number seed is identical to that used for generating the f and a realizations from which the solutions in Fig. 1 were obtained. Labeling as in Fig. 1.

The same observation is not made for the analytical, linearized head solution. Also, in the non-linear head solutions, the change from increasingly wet to increasingly dry at the locations of the wettest areas (least tension, largest head) becomes more abrupt giving the h_{NL} gray-scale map in Fig. 2 its characteristic sharp contrasts.

As a consequence, the numerical, non-linear realizations of q_1 and q_2 for $\sigma_y^2 \geq 0.5$ are significantly different in their spatial patterns from the linearized solution, even though the general locations of areas of relatively lower or higher Darcian velocities are preserved. The non-linear longitudinal Darcian velocity map $q_{1.NL}$ of a highly variable flow field (Fig. 2) shows a characteristic preferential flow pattern, previously described in Moreno et al. (1989) and Harter (1994). A braided network of channels characterizes flow at higher variances of y. The majority of flow takes place in these channels. Preferential flow channels are surrounded by relatively larger areas of the soil cross-section that contribute very little to the overall flow, i.e. have relatively small longitudinal and transverse velocities.

Plotting the absolute values of the non-linear, transverse Darcian velocity $q_{2.NL}$ yields a map with very similar patterns as the non-linear, longitudinal Darcian

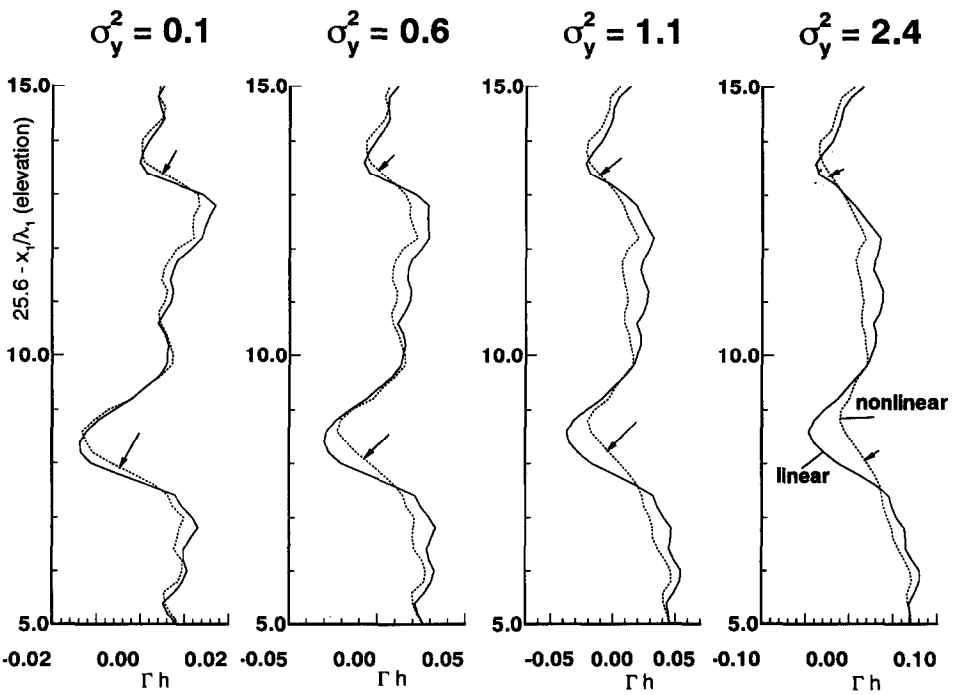

Fig. 3. Unsaturated flow: vertical cross-section of the dimensionless pressure head perturbation profile at $x_2/\lambda_2 = 15$. The linearized solution is plotted as solid curve, the numerical, non-linear solution as dotted curve. Arrows indicate portions of the pressure head cross-sections, where, with increasing variance σ_y^2, the slope of non-linear solution significantly deviates from the slope observed for the linear solution. All realizations are based on the same random number seed.

velocity, indicating a significant correlation between the absolute values of the two flux components. No such correlation between the linearized flux components $q_{1.L}$ and $q_{2.L}$ is observed. From the maps of $q_{1.NL}$ and $q_{2.NL}$ in Fig. 2 it is seen that the largest transverse fluxes (in either the positive or negative direction) occur in the preferential flow channels where longitudinal fluxes are also large, because the channels are not parallel to the x_1 axis but meander randomly back and forth around the mean flow direction. In those portions of the channels which have a significant angle against the mean flow direction, the transverse velocity component must be very large for continuity reasons.

The preferential flow channels in the non-linear solution are relatively well defined and contrast starkly with the surrounding low-velocity areas giving the velocity maps the character of a very focused picture when compared with the rather 'blurry' map of the analytical velocity components. Very similar observations are made for the realization of h, q_1, ad q_2 in a saturated flow field with reciprocal anisotropy structure in f (Fig. 4).

3.3. Statistical evaluation

The mean square error (MSE) of the linearized solutions, i.e. the mean squared difference between the linear and non-linear solutions of h, q_1, and q_2 are averaged

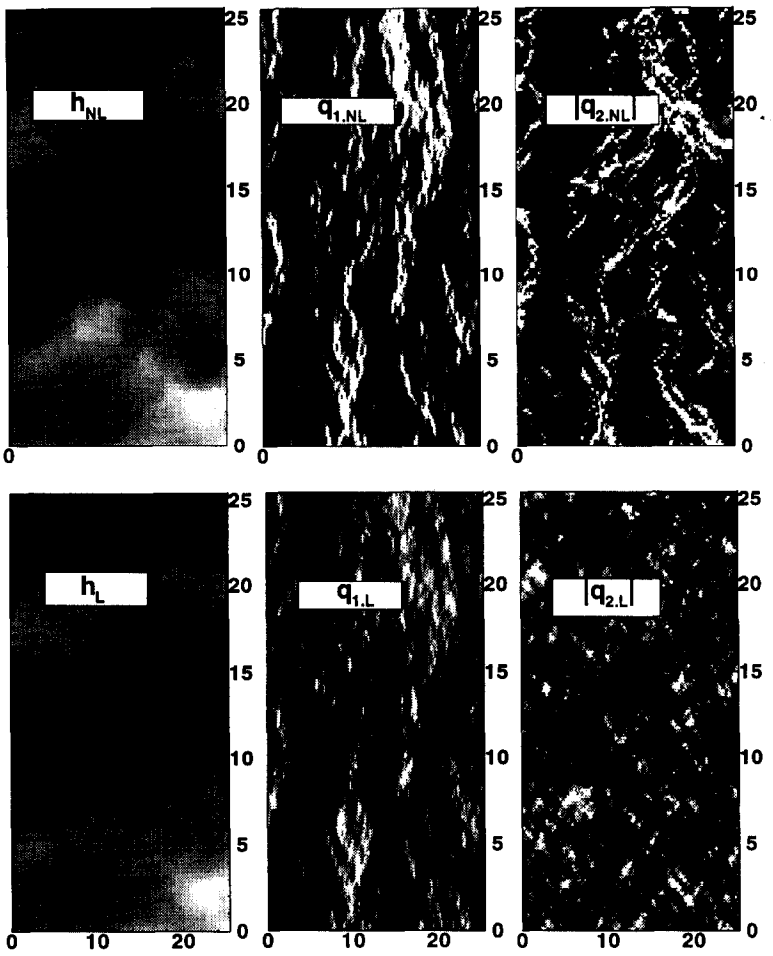

Fig. 4. Saturated horizontal flow, strong spatial heterogeneity ($\sigma_y^2 = 1.8$): realization of a linearized and non-linear head and flux solution, given the same random field realization of f. The non-linear solutions are in the top row, the linearized solutions in the bottom row. Labeling and relative grayscale as in Fig. 1. The direction of mean flux is again from top to bottom. In contrast to Fig. 2, the anisotropy ratio is $\lambda_1/\lambda_2 = 2.0$.

over the interior of the domain (excluding a zone of six columns and six rows along the boundary of the domain) and over 50 realizations. The result is normalized with respect to the linear variance of each RFV, respectively (Fig. 5). Owing to the linearization, the normalized MSE increases with the input variances σ_y^2 (unsaturated flow) and σ_f^2 (saturated flow). In the unsaturated example, normalized MSE is higher than in the saturated example. A possible explanation is the linearization of Eq. (8), which affects only the linearized solution to unsaturated flow. MSE of the flux solutions are significantly higher than those of the head solutions in both saturated and unsaturated flow. For strongly heterogeneous porous media, average differences between linear and non-linear flux solutions are of the same order as the (linear)

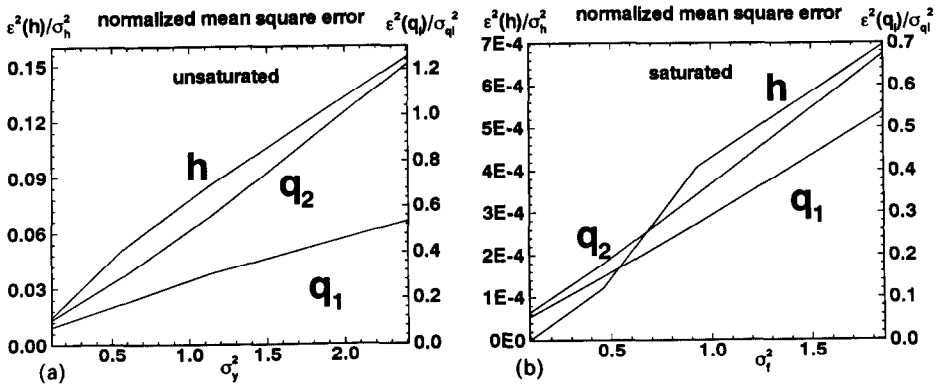

Fig. 5. Normalized mean square error of the analytical, linear solutions h, q_1, and q_2 for unsaturated flow (a) and saturated flow (b) as a function of the input variance.

spatial variability of the flux solution, which confirms the qualitative assessment made in the previous section. Such large MSE is partially caused by differences in probability density function (pdf). The linear pdf for both head and flux components is by definition Gaussian. The sample pdf of non-linear head values is also approximately normal. In contrast, we found that the non-linear flux components yield a strongly skewed sample pdf. The longitudinal flux behaves, in fact, like a log–normal pdf.

To further illustrate the differences between linear and non-linear solutions, we compare the sample variances of h, q_1, and q_2 for both the unsaturated and saturated flow case as a function of σ_y^2 and σ_f^2, respectively. The sample variances are calculated as average of the sample spatial variances of 50 independent realizations. We refer to the sample variance of the linearized solutions as 'linear sample variance' and to the sample variance of the non-linear solutions as 'non-linear sample variance'.

In the unsaturated flow case, the linear sample variance is almost directly proportional to σ_y^2 (the ensemble variance is exactly proportional if ζ is constant). With increasing spatial variability of f and a, the non-linear head variance, in contrast,

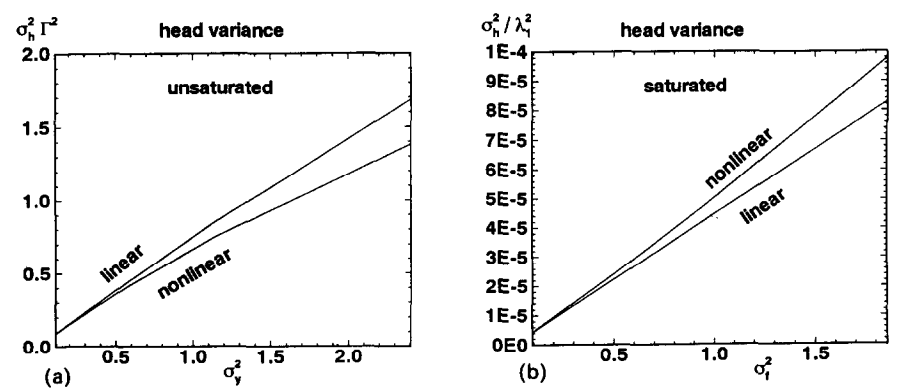

Fig. 6. Average normalized head variance of the unsaturated flow examples (a) and the saturated flow examples (b) as a function of the input variance.

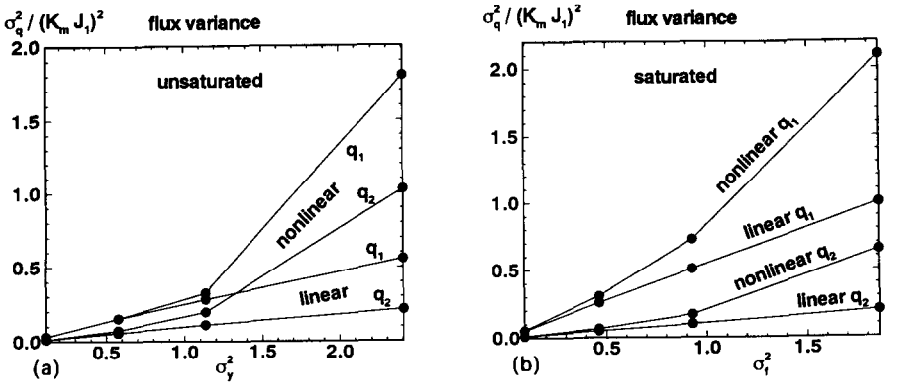

Fig. 7. Average normalized flux variance of the unsaturated flow examples (a) and the saturated flow examples (b) as a function of the input variance.

does not increase as fast as the linear head variance (Fig. 6(a)). Differences become significant for variances larger than $\sigma_y^2 \approx 0.5$. At $\sigma_y^2 = 2.4$ the non-linear head variance is approximately 20% lower than the linear head variance.

For saturated flow, the relative differences between linear and non-linear head variance are approximately the same, but with the non-linear head variance being larger than the linear head variance (Fig. 6(b)) owing to an aspect ratio υ larger than 1. Harter (1994) determined empirically that differences between the variances of h_L and h_{NL} are negligible only for $\nu = 1$ (isotropic media), even in highly variable flow fields ($\sigma_y^2 = 3.2$).

Unsaturated and saturated flux variances are significantly higher in the non-linear solutions (Fig. 7). Again, the sample variances of the linearized solution are directly proportional to the input variance of f (and a). The sample variance for the non-linear flux matches well with the sample variance from the linearized solution, if the flow variability is small ($\sigma_y^2 = \sigma_f^2 = 0.1$), but increases with higher input variances of f (and a). At large variances ($\sigma_y^2 = 2.4$ for unsaturated flow and $\sigma_f^2 = 1.8$ for saturated flow), the non-linear variance of both flux components exceeds the linearly obtained variance by a factor 2–3.

Significant differences are also observed for the mean longitudinal flux. The mean of the linearized longitudinal flux is practically constant owing to the negligible change in ζ between the different experiments (Table 1). The mean of the non-linear, unsaturated flux solution decreases by up to 15% (Fig. 8(a)) while the mean of the non-linear, saturated flux increases by over 20% in highly variable porous media (Fig. 8(b)). The differences between the unsaturated and the saturated case are again caused by the fact that the anisotropy ratios are reciprocally identical. These findings are in agreement with Yeh et al. (1985b) who derived an effective hydraulic conductivity based on a mixed first- and second-order perturbation approach. They have shown that the ratio K_e/K_m of the effective hydraulic conductivity K_e (to which the mean flux is proportional) and the geometric mean hydraulic conductivity K_m (the effective hydraulic conductivity to first order, see Eq. (12)) is equal to or greater than 1 for aspect ratios $\nu \gg 1$ and

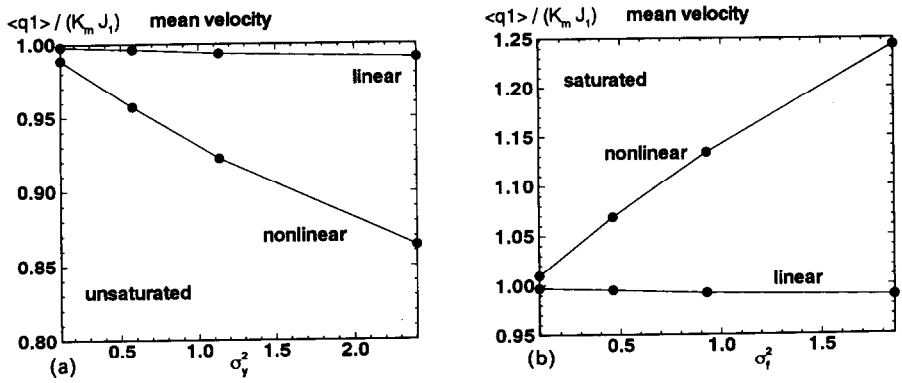

Fig. 8. Mean normalized longitudinal velocity of the unsaturated flow examples (a) and the saturated flow examples (b) as a function of the input variance.

smaller than 1 for $\nu \leq 1$ unless $\Gamma\lambda_1$ is very large. For a more detailed discussion of the differences between linear and non-linear stochastic solutions of h, q_1, and q_2, the reader is referred to Harter (1994).

4. Application to transport simulation

Just for its own sake, the Monte Carlo simulation of h and $\boldsymbol{q}$ by the linearized cosimulation method is of little practical use. All moments of h and $\boldsymbol{q}$ can be derived analytically (Bakr et al., 1978; Gutjahr et al., 1978; Yeh et al., 1985a, b; Harter, 1994). Cosimulated h and $\boldsymbol{q}$ realizations can only be advantageous when used as input to the Monte Carlo analysis of other random field variables such as the displacement of solute particles, the travel time of solute particles, the concentration of a solute plume, or the soil moisture distribution. As an example of such an application, the solute displacement and solute travel time are computed numerically given the flux field $\boldsymbol{q}_{\mathrm{L}}$. The results are compared with those transport results obtained from the non-linear flux field $\boldsymbol{q}_{\mathrm{NL}}$.

Such simulations have in the past often been used to determine the macrodispersion of solutes in heterogeneous porous media. Bellin et al. (1992) compared the results of numerical simulations (non-linear flow and non-linear transport) with a number of other combined flow and transport models, some of which are linear, some non-linear. Analytical, linearized transport models have been proposed to compute the macrodispersion and travel time distribution of solutes (Dagan, 1982, 1984, 1988; Gelhar and Axness, 1983; Neuman et al., 1987; Cvetkovic et al., 1992; Dagan et al., 1992). Non-linear, semi-analytical transport models have been suggested more recently (Rubin, 1990; Neuman and Zhang, 1990; Zhang and Neuman, 1995). Here, a numerical transport model is used for the non-linear analysis of solute particle transport to assess the effect of linearizing the flow equation as suggested in the previous section.

Particle transport is computed for each realization $\boldsymbol{q}_{\mathrm{L}}$ and $\boldsymbol{q}_{\mathrm{NL}}$. An explicit forward particle tracking method is employed

$$x_j(t^{m+1}) = x_j(t^m) + \frac{q_i[\boldsymbol{x}(t^m)]}{\theta}\Delta t^m \qquad j = 1,2 \tag{30}$$

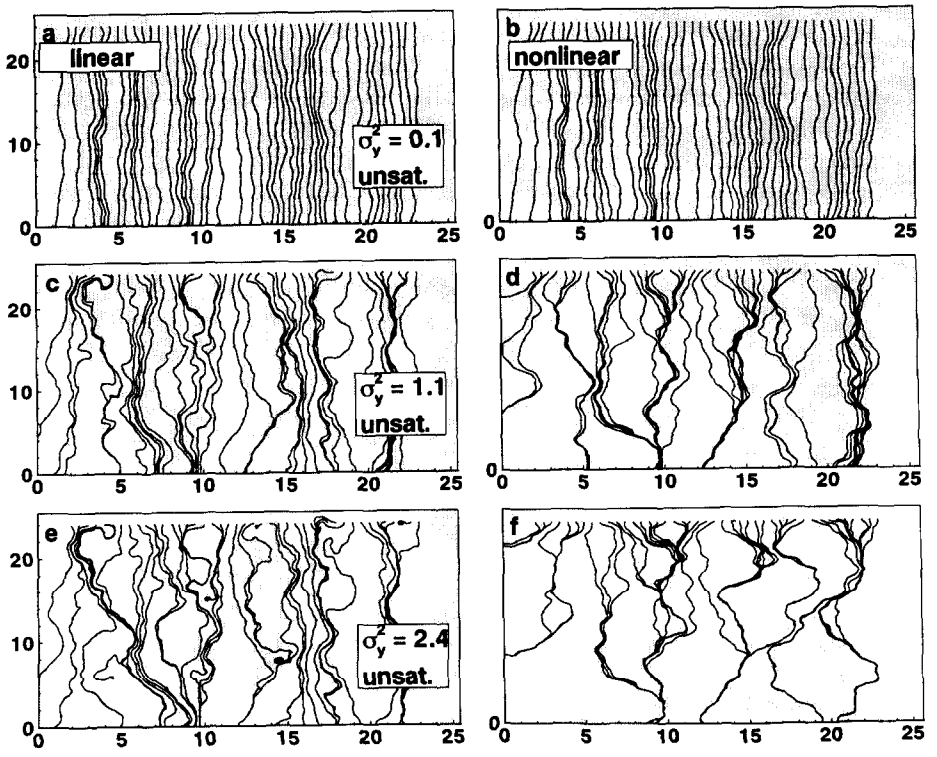

Fig. 9. Unsaturated flow: realization of streamlines using the linearized flux realization (a) (c) and (e) and the non-linear flux realization (b) (d) and (f) at different variances of y: 0.1 (a and b), 1.1 (c and d), and 2.4 (e and f). Axes labeling as in Fig. 1. Mean flow is vertically downward.

The flux q_L between the grid points of the cosimulated realization and the flux q_{NL} between the nodes of the finite element solution is computed through bilinear weighting. The time-step Δt^m is determined such that at each step the particle moves by 1/4 of the distance between grid points or nodes in one of the two directions and by less than 1/4 of the grid or node spacing in the respective other direction. Three particles are tracked through each realization. All of them are inserted at a distance $2\lambda_1$ from the upstream boundary. The first particle is inserted upstream from the center of the simulated domain, the other two particles are injected at a lateral distance $3\lambda_2$ on each side of the first particle. The particle arrival time at the outflow boundary is used for statistical analysis. For each set of input variances (Table 1), 50 Monte Carlo simulations (MCS) are implemented, resulting in 150 quasi-uncorrelated particle trajectories.

At small variances ($\sigma_y^2 = 0.1$) the travel paths based on q_L and on q_{NL} are practically identical (Figs. 9 (a) and (b)). Significant differences are seen in the travel paths of particles at moderate variances ($\sigma_y^2 = 1.0$) (Figs. 9 (c) and (d)). At even larger variances, the travel paths of many particles in the q_L realization indicate non-zero curl in the analytical solution q_L, i.e. q_L is not free of artificial sinks or sources

(Figs. 9 (e) and (f)). The observed artificial sinks are not due to the transport model, since they do not occur if $\boldsymbol{q}_{NL}$ is used as flux field. Mass balance is conserved owing to the particular formulation of both analytical and numerical solutions: the first-order perturbation equation (11) is mass-conservative and the finite element formulation for the non-linear solution is based on a mass-balance equation. The curl in the linear (Eulerian) flux field, which can be caused by even small mass-balance errors must therefore be explained by the discrete evaluation of Eq. (22) and the fact that the linear solution does not preserve the strong correlation of $\log|q_1|$ and $\log|q_2|$ found for the nonlinear flux field.

Not only are the travel paths based on the non-linear solution curl-free, they are distinctly different from those computed for the linearized flux field. The most important difference is the stronger clustering of travel paths along the preferential flow channels shown in Fig. 2. The clustering of travel paths is much weaker in the linear flux based solutions (Fig. 9(e)). This result is expected given the different nature of the $\boldsymbol{q}_L$ and $\boldsymbol{q}_{NL}$ realizations (see above).

In many applications, the character of the individual travel paths is of much less interest then some stochastic measures about the ensemble of travel paths or the ensemble of the associated travel times. Here, the sample cumulative distribution function (CDF) of arrival times at a distance $x_1 = 23.6\lambda_1$ are studied. They are found to be highly skewed both for linear flux based particles (CDF_L) and for non-linear flux based particles (CDF_{NL}). Fig. 10 therefore shows the sample CDF of the logarithms (natural log) of the arrival time. At very small variances ($\sigma_y^2 = 0.1$) the CDF_L matches very well with the CDF_{NL}. At large variances of y and f, small differences are observed between CDF_L and CDF_{NL}, which mainly reflect the observed differences in mean flux. But for practical purposes CDF_L gives a very good approximation of CDF_{NL}. The relative insensitivity of the CDF to the type of flux solution has several reasons.

(1) only the arrival times of particles that arrive at the bottom boundary are included in the statistical analysis; particles that end in artificial sinks of the $\boldsymbol{q}_L$ flux field are ignored.

(2) the arrival time CDF is integrated over the entire width of the outflow boundary, which makes it insensitive to the transverse spatial distribution of the particle arrival location.

5. Conclusion

For the Monte Carlo simulation of unsaturated and saturated flow in heterogeneous porous media a cosimulation technique has been developed that generates not only random fields of the saturated hydraulic conductivity and the soil pore size distribution parameter, but also cogenerates the first-order perturbation solutions h to the general flow equation (1) with Eq. (3) defining $K(h)$, and the corresponding solutions q_1 and q_2 to Darcy's law. The cosimulator is an extended spectral random field generator, which takes advantage of spectral perturbation analysis of saturated

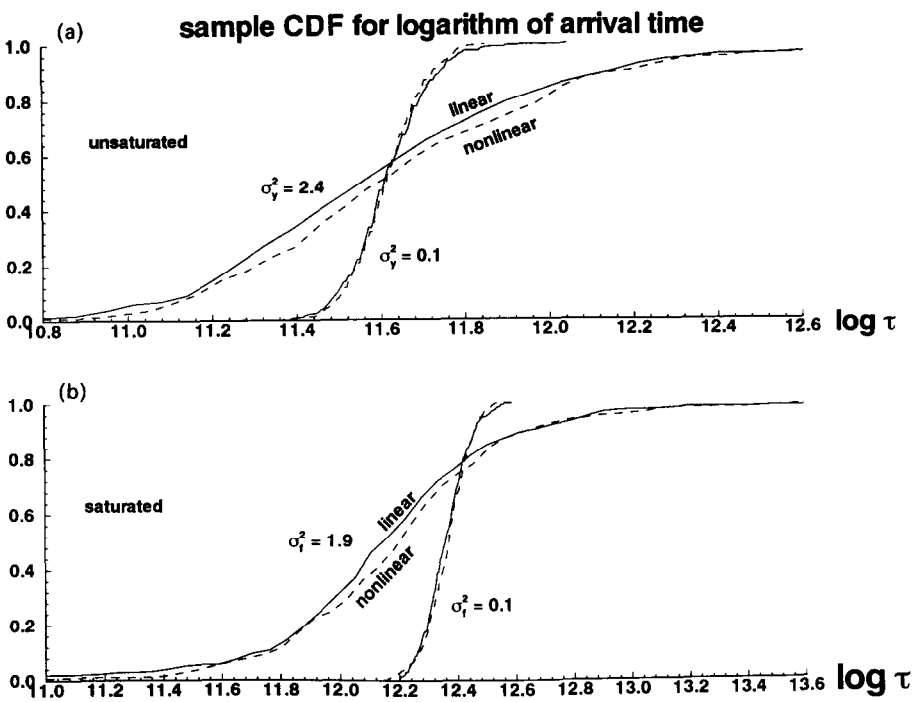

Fig. 10. Sample cumulative distribution functions (CDF) of the arrival time of particles at the exit boundary (lower boundary in Fig. 9) for unsaturated flow (a) and saturated flow (b) in mildly and strongly heterogeneous porous media: comparison of the CDF obtained from the linearized flux field realizations (solid lines) and the CDF obtained from the finite element, non-linear flux realizations (dashed lines).

and unsaturated flow. Spectral analysis gives explicit spectral solutions to the first-order perturbation flow equation, which is a linearized PDE, whether flow is saturated or unsaturated. It also gives an explicit solution to the first-order perturbation form of Darcy's law. The spectral representations of f, a, h, and $\boldsymbol{q}$ are transformed to spatial random fields by FFT.

For moderate variability in the flow field ($\sigma_y^2 < 1, \sigma_f^2 < 1$), the linear solutions h_L and $\boldsymbol{q}_L$ are very robust and should for many practical purposes be useful, since they can be computed in a fraction of the time necessary for the numerical, non-linear solutions h_{NL} and $\boldsymbol{q}_{NL}$. For the unsaturated case, the reduction in computation time is up to three orders of magnitude. For saturated flow, the increase in computational efficiency is between one and two orders of magnitude.

The application of the cosimulation procedure to the stochastic analysis of transport in heterogeneous, porous media was investigated. For moderately heterogeneous porous media, the travel paths of particles based on the linear flux field are very similar to those particle travel paths based on the non-linear flux field. For porous media of moderate variability, the cosimulated, linearized solutions of h and $\boldsymbol{q}$ are therefore a computationally efficient alternative to numerical models for implementing Monte Carlo simulations of solute transport. If the hydraulic conductivity

variability is very strong, non-linear flux fields are highly skewed and have strong preferential flow channels, which cannot be modeled with a linearized approach. This leads to distinctly different travel patterns of solute particles in the linear and non-linear flux field. In addition, the linear flux-field is not found to be free of curl. Artificial sinks and sources are therefore common and lead to mass-balance problems in the transport solution. However, the arrival time distribution of solute particles is not very sensitive to the differences between q_L and q_{NL}. The computation of the arrival time CDF is an example of an application, where linearized cosimulation can successfully be applied even to very heterogeneous porous media.

Acknowledgments

We gratefully acknowledge the thorough and thoughtful comments and corrections given by one of the anonymous reviewers. This study is funded by a research grant from the Subsurface Science Program, Environmental Sciences Division, US Department of Energy, under Grant No. DE-FG02-91ER6119.

References

Ababou, R., McLaughlin, D., Gelhar, L.W. and Tompson, A.F.B., 1989. Numerical simulation of three-dimensional saturated flow in randomly heterogeneous porous media. Transp. Por. Med., 4: 549–565.

Bakr, A.A., Gelhar, L.W., Gutjahr, A.L. and McMillan, J.R., 1978. Stochastic analysis of the effect of spatial variability in subsurface flows, 1: Comparison of one- and three-dimensional flows. Water Resour. Res., 14: 263–271.

Bellin, A., Salandin, P. and Rinaldo, A., 1992. Simulation of dispersion in heterogeneous porous formations: statistics, first-order theories, convergence of computations. Water Resour. Res., 28: 221–2227.

Brigham, E.O., 1988. The Fast Fourier Transform and its Applications. Prentice Hall, Englewood Cliffs, NJ.

Cvetkovic, V., Shapiro, A.M. and Dagan, G., 1992. A solute flux approach to transport in heterogeneous formations, 2. Uncertainty analysis. Water Resour. Res., 28: 1377–1388.

Dagan, G., 1979. Models of groundwater flow in statistically homogeneous porous formations. Water Resour. Res., 15: 47–63.

Dagan, G., 1982. Stochastic modeling of groundwater flow by unconditional and conditional probabilities, 2. The solute transport. Water Resour. Res., 18: 835–848.

Dagan, G., 1984. Solute transport in heterogeneous porous formations. J. Fluid Mech., 145: 151–177.

Dagan, G., 1988. Time-dependent macrodispersion for solute transport in anisotropic heterogeneous aquifers. Water Resour. Res., 24: 1491–1500.

Dagan, G., Cvetkovic, V. and Shapiro, A.M., 1992. A solute flux approach to transport in heterogeneous formations, 1. The general framework. Water Resour. Res., 28: 1369–1376.

Gardner, W.R., 1958. Some steady state solutions of unsaturated moisture flow equations with applications to evaporation from a water table. Soil Sci., 85: 228–232.

Gelhar, L.W. and Axness, C.L., 1983. Three-dimensional stochastic analysis of macrodispersion in aquifers. Water Resour. Res., 19: 161–180.

Gutjahr, A.L., 1989. Fast Fourier transforms for random field generation. In: Project Report for Los Alamos Grant to New Mexico Tech, Contract Number 4-R58-2690R. Department of Mathematics, New Mexico Tech, Socorro, NM.

Gutjahr, A.L., Gelhar, L.W., Bakr, A.A. and McMillan, J.R., 1978. Stochastic analysis of spatial variability in subsurface flows. Part II: Evaluation and application. Water Resour. Res. 14: 953–960.

Gutjahr, A.L., Hatch, S., Bullard, B. and Hughson, L., 1993. Conditional simulation and contaminant flow modeling. Technical Completion Rep. New Mexico Institute of Mining and Technology, Socorro, NM, Project No. WERC 91-08.

Gutjahr, A.L., Bullard, B., Hatch, S. and Hughson, L., 1995. Joint conditional simulations and the spectral approach for flow modeling. J. Stoch. Hydrol. Hydraul., 8: 79–108.

Harter, Th., 1994. Unconditional and conditional simulation of flow and transport in heterogeneous, variably saturated porous media. Ph.D. Dissertation, University of Arizona, Tucson, AZ.

Harter, Th. and Yeh, T-C.J., 1993. An efficient method for simulating steady unsaturated flow in random porous media: using an analytical perturbation solution as initial guess to a numerical model. Water Resour. Res., 29: 4139–4149.

Koopmans, L.H., 1974. The Spectral Analysis of Time Series. Academic.

Lumley, J.L. and Panofsky, H.A., 1964. The Structure of Atmospheric Turbulence. John Wiley.

Mantoglou, A. and Gelhar, L.W., 1987a. Stochastic modeling of large-scale transient unsaturated flow systems. Water Resour. Res., 23: 37–46.

Mantoglou, A. and Gelhar, L.W., 1987b. Capillary tension head variance, mean soil moisture content, and effective specific soil moisture capacity of transient unsaturated flow in stratified soils. Water Resour. Res., 23: 47–56.

Mantoglou, A. and Gelhar, L.W., 1987c. Effective hydraulic conductivities of transient unsaturated flow in stratified soils. Water Resour. Res., 23: 57–67.

Moreno, L., Tsang, Y.W., Tsang, C.F., Hale, F.V. and Neretnieks, I., 1989. Flow and tracer transport in a single fracture: A stochastic model and its relation to some field observations. Water Resour. Res., 24: 2033–2048.

Naff, R.L. and Vecchia, A.V., 1987. Depth-averaging effects on hdyraulic head for media with stochastic hydraulic conductivity. Water Resour. Res., 23: 561–570.

Neuman, S.P. and Zhang, Y.-K., 1990. A quasi-linear theory of non-Fickian and Fickian subsurface dispersion, 1. Theoretical analysis with application to isotropic media. Water Resour Res., 26: 887–902.

Neuman, S.P., Winter, C.L. and Newman, C.M., 1987. Stochastic theory of field-scale Fickian dispersion in anisotropic porous media. Water Resour. Res., 23: 453–466.

Priestley, M.B., 1981. Spectral Analysis and Time Series. Academic, San Diego, pp. 890.

Robin, M.J.L., Gutjahr, A.L., Sudicky, E.A. and Wilson, J.L., 1993. Cross-correlated random field generation with the direct Fourier transform method. Water Resour. Res., 29: 2385–2397.

Rubin, Y., 1990. Stochastic modeling of macrodispersion in heterogeneous porous media. Water Resour. Res., 26: 133–141.

Rubin, Y. and Dagan, G., 1987a. Stochastic identification of transmissivity and effective recharge in steady groundwater flow, 1: Theory. Water Resour. Res., 23: 1185–1192.

Rubin, Y. and Dagan, G., 1987b. Stochastic identification of transmissivity and effective recharge in steady groundwater flow, 2. Case study. Water Resour. Res., 23: 1193–1200.

Rubin, Y. and Dagan, G., 1988. Stochastic analysis of boundaries effects on head spatial variability in heterogeneous aquifers, 1. Constant head boundary. Water Resour. Res., 24: 1689–1697.

Rubin, Y. and Dagan, G., 1989. Stochastic analysis of boundaries effects on head spatial variability in heterogeneous aquifers, 2. Impervious boundary. Water Resour. Res., 25: 707–712.

Smith, L. and Freeze, R.A., 1979a. Stochastic analysis of groundwater flow in a bounded domain, 1: One-dimensional simulations. Water Resour. Res., 15: 521–528.

Smith, L. and Freeze, R.A., 1979b. Stochastic analysis of groundwater flow in a bounded domain, 2. Two-dimensional simulations. Water Resour. Res., 15: 1543–1559.

Tompson, A.F.B. and Gelhar, L.W., 1990. Numerical simulation of solute transport in three-dimensional, randomly heterogeneous porous media. Water Resour. Res., 26: 2541–2562.

Tompson, A.F.B., Ababou, R. and Gelhar, L.W., 1989. Implementation of the three-dimensional turning bands random field generator. Water Resour. Res., 25: 2227–2243.

Wierenga, P.J., Toorman, A.F., Hudson, D.B., Vinson, J., Nash, M. and Hills, R.G., 1989. Soil physical properties at the Las Cruces trench site. US Nuclear Regulatory Commission, Washington, DC, NUREG/CR-5441.

Yeh, T.-C.J., Gelhar, L.W. and Gutjhar, A.L., 1985a. Stochastic analysis of unsaturated flow in heterogeneous soils, 1: Statistically isotropic media. Water Resour. Res., 21: 447–456.

Yeh, T.-C.J., Gelhar, L.W. and Gutjahr, A.L., 1985b. Stochastic analysis of unsaturated flow in heterogeneous soils, 2: Statistically anisotropic media with variable α. Water Resour Res., 21: 457–464.

Yeh, T-C.J., Gelhar, L.W. and Gutjahr, A.L., 1985c. Stochastic analysis of unsaturated flow in heterogeneous soils, 3: Observations and applications. Water Resour. Res., 21: 465–471.

Yeh, T-C.J., Srivastava, R., Guzman, A. and Harter, Th., 1993. A numerical model for two-dimensional water flow and chemical transport. Ground Water, 32: 2–11.

Van Lent, Th. and Kitanidis, P.K., 1989. A numerical spectral approach for the derivation of piezometric head covariance functions. Water Resour. Res., 25: 2287–2298.

Zhang, D. and Neuman, S.P., 1995. Eulerian-Lagrangian analysis of transport conditioned on hydraulic data: 1. Analytical-numerical approach. Water Resour. Res., 31: 39–51.